Nanoscale

Accepted Manuscript

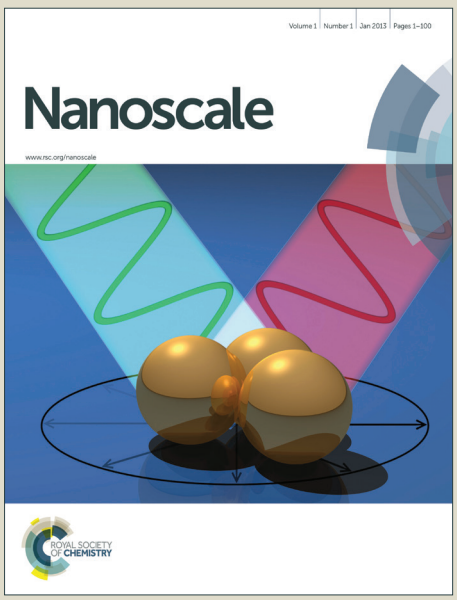

ROYAL SOCIETY OF CHEMISTRY

www.rsc.org/nanoscale

Cite this: DOI: 10.1039/c0xx00000x

www.rsc.org/xxxxxx

ARTICLE TYPE

Sustainable Molecular Oxygen Activation with Oxygen Vacancies on the {001} Facets of BiOCl Nanosheets under Solar Light

Hao Li, Jingu Shi, Kun Zhao and Lizhi Zhang*

Received (in XXX, XXX) Xth XXXXXXXXX 20XX, Accepted Xth XXXXXXXXX 20XX

DOI: 10.1039/b000000x

We demonstrate that oxygen vacancies on the {001} facets of BiOCl nanosheets can more sustainably activate molecular oxygen for organic pollutant removal under solar light than the TiO_2 counterparts. The oxygen vacancies on the {001} facets of BiOCl nanosheets are effectively refreshed by UV light, and also responsible for the efficient utilization of visible light to activate molecular oxygen, accounting for their long term stability and high efficiency.

Photocatalytic molecular oxygen activation is related to the surface chemistry of the oxide semiconductors and thus highly dependent on the interaction between molecular oxygen and oxide surface. It is widely accepted that molecular oxygen interacts weakly with fully oxidized surface, but can be easily charged by the localized electrons at oxygen vacancies (OVs) on the surface. Interaction of molecular oxygen with oxide surface proceeds mainly through molecular oxygen activation and dissociation channels.[1] For example, O_2 can be chemisorbed on the OVs of TiO_2 in the forms of $\bullet O_2^-$, O_2^{2-}, or O_4^{2-}, depending on the coverage and the adsorption geometry of O_2 as well as the location of OVs.[2-5] The molecularly chemisorbed states of O_2 is the first important and critical step for the molecular oxygen activation to generate reactive oxygen species (ROS) in the presence of external excitation such as light irradiation during the molecular oxygen activation channel. As for the dissociative channel, the molecular oxygen dissociation is theoretically and experimentally favorable on the OVs of reduced TiO_2, as triggered by elevated temperature, high volts of scanning tunneling microscope or light irradiation, where typically one O atom heals a bridging vacancy, while the other O atom resides as an adatom on the surface.[6-7] In view of the concurrence of molecular oxygen activation and dissociation channels, the atomic-level healing of OVs during the dissociative channel would macroscopically reoxidize the oxide surface, and thus block the molecular oxygen activation channel, leading to the termination of molecular oxygen activation. Therefore, the stability and the regeneration of OVs are vital for the long term photocatalytic molecular oxygen activation, which has been seldom studied.

Bismuth oxychloride (BiOCl) of unique layered structure has attracted increasing attention.[8-11] Recently, we found that the OVs on the (001) surface of BiOCl preferred to reduce molecular oxygen to $\bullet O_2^-$ through one-electron transfer, while the OVs on the (010) surface favored the formation of O_2^{2-} via two-electron transfer, which was co-governed by the surface atom exposure and the *in situ*-generated OV characteristics of the (001) and (010) surfaces under UV light irradiation.[9] However, the wide indirect-transition optical bandgap of about 3.3 eV limits the molecular oxygen activation performance of BiOCl under solar light of less than 5% UV light. Although it is known that the presence of OVs can enhance the photoreactivity of BiOCl under visible light,[10-11] the intrinsic roles of OVs on the solar light-driven molecular oxygen activation with BiOCl and its long term stability are never investigated previously to the best of our knowledge.

In this communication, we demonstrate that OVs on the {001} facets of BiOCl nanosheets can much more sustainably activate molecular oxygen for organic pollutant removal under solar light than the TiO_2 counterparts. The intrinsic roles of OVs during molecular oxygen activation are clarified through exploring the relationship between the OVs concentration and the photocatalytic molecular oxygen activation performance of BiOCl. We also propose a possible mechanism to explain the interesting long term stability of OVs on the {001} facets of BiOCl anosheets for the molecular oxygen activation under solar light.

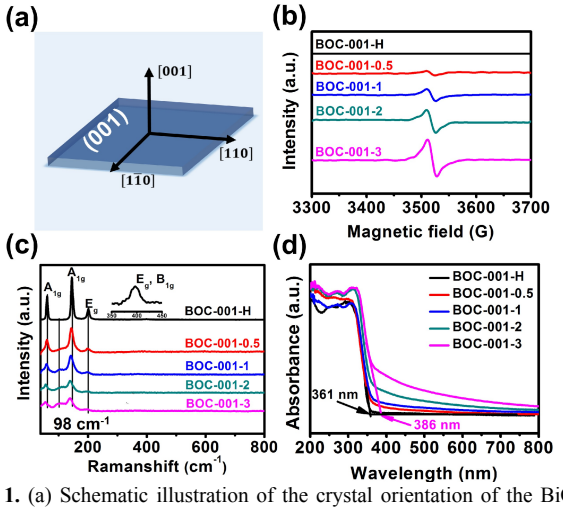

Fig. 1. (a) Schematic illustration of the crystal orientation of the BiOCl single-crystalline nanosheet with {001} facets exposed. (b) EPR spectra, (c) Raman spectra, and (d) UV-vis absorption spectra of the as-prepared BiOCl photocatalysts.

The selective generation of OVs on the {001} facets of BiOCl nanosheets was realized through the redox reaction between the

{001} facets of BiOCl and hot ethylene glycol.[12-13] We called the resulting samples as BOC-001-x (x = 0.5, 1, 2, and 3, which represented the millimole quantities of bismuth precursor). For comparison, we annealed BOC-001-3 in the air at 300 °C to obtain a reference photocatalyst without OVs, which was denoted as BOC-001-H. Electron microscope images first revealed the all the as-prepared BiOCl were assembled by radically grown single-crystalline nanosheets with exposed {001} facets (Fig. 1a, S1 and S2, ESI†), while the generation of OVs on the {001} facets seriously weakened the X-ray diffraction peaks of (00L) planes (Fig. S3, ESI†). Low-temperature electron paramagnetic resonance (EPR) analysis showed that all BOC-001-x possessed a typical signal at g = 2.001, corresponding to the existence of OVs with the intensity increasing from BOC-001-0.5 to BOC-001-3 (Fig. 1b). After the OVs generation on the {001} facets, Raman spectra of BOC-001-x exhibited three distinct changes including the peak intensity decrease and the blue shift of vibration peak as well as the appearance of a new peak at 98 cm^{-1} (Fig. 1c). The peak intensity decrease was caused by the crystallinity weakening, while the blue shift and the appearance of the new peak were arisen from the OVs and the lower charge Bi ions of $Bi^{(3-x)+}$ in the sample, respectively.[9] X-ray photoelectron spectroscopy (XPS) analysis revealed that two additional peaks with lower binding energies at 163.8 and 158.5 eV appeared in the Bi 4f high resolution spectra of BOC-001-x, which were arisen from $Bi^{(3-x)+}$ (Fig. S4, ESI†).[10] As the lower charge Bi ions corresponded to the oxygen atoms loss, the OVs concentrations in BOC-001-x were proportional to the percentages of $Bi^{(3-x)+}$. These characterization results revealed that the concentration of OVs on the {001} facets of BiOCl could be easily tuned with changing the amount of bismuth precursor during the synthesis, enabling us to investigate the intrinsic roles of OVs during the solar light-driven molecular oxygen activation.

To clarify the roles of OVs on the {001} facets of BiOCl nanosheets during the solar light-driven molecular oxygen activation, we first investigated the optical properties of BOC-001-x, as the OVs-induced sub-band excitation from defect states to the conduction band (CB) would significantly change the optical properties of oxide semicondutors.[14-15] Different from white color of BOC-001-H, the colors of BOC-001-x gradually changed from pale-grey to yellowish-brown with increasing the amount of OVs (Fig. S5a, ESI†). The color change of BOC-001-x was also reflected by the continuous and exponentially decaying absorption tails across the whole visible light region of UV-vis absorption spectra (Fig. 1d). Besides the absorption tails, BOC-001-3 also possessed a distinct band edge red-shifting from 361 to 386 nm corresponded to a band gap narrowing. This band gap narrowing might be attributed to the overlapping of the OVs' electronic states with the semiconductors' band edge at the high concentration of OVs (Fig. 1d).[16-17]

Further density of electronic states calculation revealed that localized electronic states composed of Bi 6p orbital appeared beneath the CB minimum after the generation of an OV on the hydrogen-stabilized {001} facet (Fig. 2a-c and S5b, ESI†). The location of the OV states suggested a shallow donor behavior, indicating that localized electrons could possibly be excited to the CB of BiOCl under visible light (Fig. 2d). To validate the sub-band excitation of the OVs-induced defect states, we monitored the transient photocurrent responses of BOC-001-x under visible light. Although the bandgap narrowing of BOC-001-2&3 red shifted their absorption edge even to 386 nm, they could not be directly excited under visible light of $\lambda > 420$ nm. Compared with BOC-001-H, BOC-001-x possessed enhanced transient photocurrents, which were therefore attributed to the presence of OVs on the {001} facets (Fig. 2e). Moreover, the maximum transient photocurrents intensity of BOC-001-3 under monochromatic light distinctly decreased with increasing the wavelength and also matched well with its absorption tail across the visible light region (Fig. 2f), confirming the indispensable contribution of OVs on the {001} facets to the visible light response of BOC-001-x.

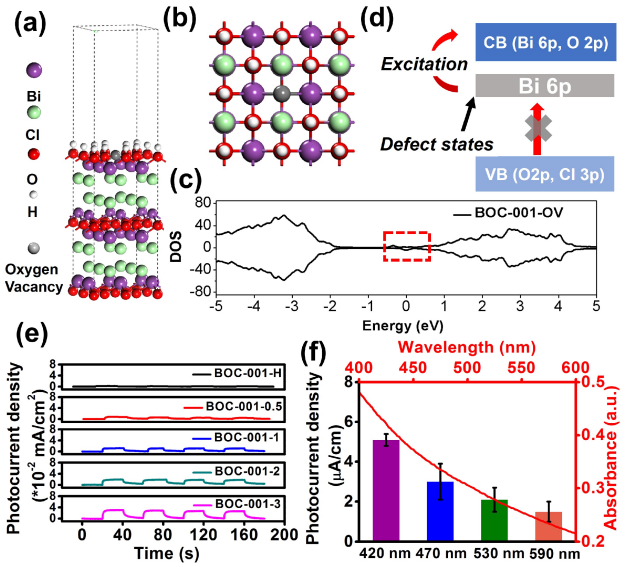

Fig. 2. Side (a) and top (b) view of the structure of hydrogen-stabilized {001} facet of BiOCl. (c) Calculated DOS for the oxygen-deficient {001} facet (the dotted box showed the defect states beneath the CB minimum). (d) Schematic illustration of the sub-band excitation. (e) Transient photocurrent responses of the as-prepared BiOCl nanosheets under visible light. (f) Maximum transient photocurrent density of BOC-001-3 under monochromatic light along with its light absorption in the visible light region.

The sub-band excitation allows the electron transfer from defect states to molecular oxygen under visible light, while the subsequent activation process is highly dependent on the adsorption states of O_2 on OVs. Our recent calculation results revealed that O_2 is chemisorbed on OVs of BiOCl {001} facets in the transitional form of $*O_2^-$.[9] To check the molecular oxygen activation process in this study, EPR was first adopted to detect the spin-reactive ROS with 5, 5-dimethyl-1-pyrroline-N-oxide (DMPO) as a spin trap in aqueous solution. Upon visible light irradiation for 3 min, a four-line spectrum with relative intensities of 1 : 1 : 1 : 1 was observed over BOC-001-3, which was the characteristic signal of the DMPO-$\bullet O_2^-$ adduct, while such a signal was not observed for BOC-001-H (Fig. 3a). As stated previously, BOC-001-3 could not be directly excited under visible light, $\bullet O_2^-$ was only arisen from the activation of chemisorbed O_2 through one-electron transfer via the sub-band excitation. Meanwhile, another four-line spectrum with relative intensities of 1 : 2 : 2 : 1 was also observed over BOC-001-3, originating from the DMPO-•OH adduct (Fig. 3a). As the photo-excited holes generated through the sub-band excitation of BOC-

001-3 have low oxidation potential and thus cannot oxidize H_2O or OH^- to •OH, the observed •OH must be produced via H_2O_2 → •OH. It is known that H_2O_2 can be generated through two possible ways of two-electron reduction through O_2 → O_2^{2-} → H_2O_2 and the one-electron reduction of $•O_2^-$ through $•O_2^-$ → O_2^{2-} → H_2O_2. In comparison with the direct two-electron reduction process, the one-electron reduction of $•O_2^-$ to O_2^{2-} requires an additional activation energy, so it is possible to judge the dominant electron transfer process by comparing the relative concentrations of $•O_2^-$ and H_2O_2.[9, 18] Therefore, we quantitatively measured the concentrations of ROS generated by BOC-001-x under visible light (Fig. S6, ESI†). It was found that the ROS gradually increased in 60 min over BOC-001-x, and the overall ROS generated after 60 min linearly increased with the percentages of $Bi^{(3-x)+}$. This confirmed that the ROS generation capacity of BOC-001-x was determined by the amount of OVs on the {001} facets (Fig. 3b). Moreover, the $•O_2^-$ generation rate was over 4 times faster than those of H_2O_2 and •OH over BOC-001-3 (Fig. 3c), further confirming that the {001} facets of BiOCl nanosheets preferred to reduce O_2 to $•O_2^-$ through one-electron transfer, and also revealing that H_2O_2 was produced mainly by the one-electron reduction of $•O_2^-$ through the $•O_2^-$ → O_2^{2-} → H_2O_2 pathway in this study.

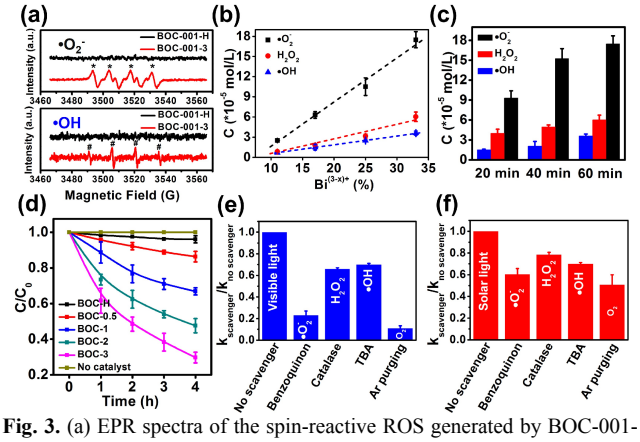

Fig. 3. (a) EPR spectra of the spin-reactive ROS generated by BOC-001-H and BOC-001-3 under visible light. (b) Concentrations of the generated ROS over BOC-001-x as a function of the corresponding $Bi^{(3-x)+}$ percentages under visible light. (c) The ROS generated over BOC-001-3 as a function of the irradiation time under visible light. (d) Photocatalytic NaPCP removal in the absence or presence of BOC-001-x under visible light. Photocatalytic removal of NaPCP in the presence of different scavengers over BOC-001-3 under visible light (e) and solar light (f).

In view of the abundance and safety as well as low cost characteristics of molecular oxygen, it is of great significance to utilize molecular oxygen activated by the OVs on the {001} facets of BiOCl nanosheets to remove organic pollutants, we therefore employed BOC-001-x to photocatalytically remove sodium pentachlorophenate (NaPCP), a typical colorless and highly toxic pollutant in water. Results revealed that NaPCP molecules did not self degrade under visible light irradiation in the absence of photocatalysts, while both visible light and OVs were necessary for the photocatalytic NaPCP removal (Fig. 3d and S7a, ESI†). The photoreactivity of BOC-001-x was proportional to the concentrations of generated ROS, which were essentially governed by the amount of OVs on the {001} facets (Fig. 3d). The indispensable role of OVs for the ROS generation and the NaPCP removal was further proven by the significantly decreased photoreactivity of BOC-001-3 coated with a layer of SiO_2 to passivate the surface defects (Fig. S7b-d, ESI†).

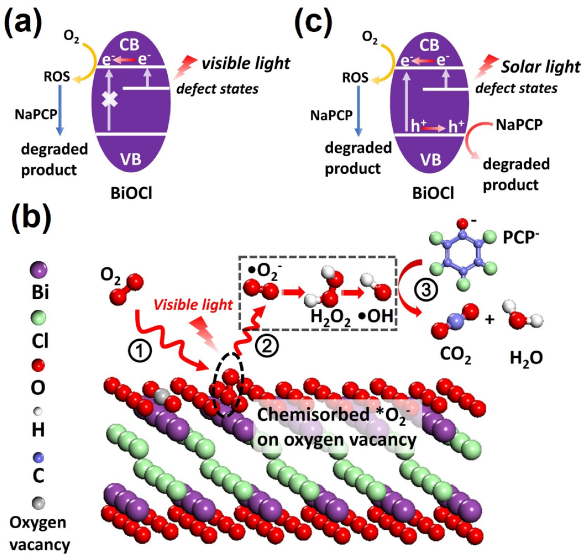

Fig. 4. (a) Proposed mechanism for the high molecular oxygen dependence over BOC-001-3 for NaPCP removal under visible light. (b) Schematic illustration of the molecular oxygen activation on the OVs of BiOCl {001} facets for NaPCP removal under visible light. (c) Proposed mechanism for photocatalytic removal of NaPCP over BOC-001-3 under solar light.

A series of experiments were then carried out to investigate the active species responsible for the NaPCP removal under visible light through adding different scavengers (p-benzoquinone for $•O_2^-$, catalase for H_2O_2, *tert*-butyl alcohol for •OH). The inhibition efficiencies were estimated to be 75% for p-benzoquinone, 34% for catalase, and 30% for *tert*-butyl alcohol (TBA) on the removal of NaPCP, indicating that the contribution of the ROS on the NaPCP removal was in the order of $•O_2^-$ > H_2O_2 > •OH, consistent with their concentrations (Fig. 3e and S8a, ESI†). Moreover, the ROS generation and the NaPCP removal over BOC-001-3 under visible light was almost completely inhibited (over 90% inhibition efficiency) when water-dissolved molecular oxygen was removed (Fig. 3e and S8b, ESI†). This revealed that the photoreacitivty of BOC-001-3 under visible light was highly dependent on the molecular oxygen activation in this study. We also interestingly found that the roles of ROS on the NaPCP removal with OVs induced sub-band excitation under visible light were quite different from that with direct excitation from valence band to CB under UV light. Under UV light, Ar purging could only inhibit 37% of the NaPCP removal efficiency close to that of $•O_2^-$, while the contributions of H_2O_2 and •OH on the NaPCP removal could be negligible, indicating that photo-generated holes played a more important role on the NaPCP removal (Fig. S8c-d, ESI†). This is because the oxidation potential of holes generated through sub-band excitation under visible light can be estimated by the standard potential of $Bi^{3+}/Bi^{(3-x)+}$, much lower than that of holes generated under UV light corresponding to the standard potential of Bi^{5+}/Bi^{3+}. Therefore, the photo-generated holes of low oxidation potential under visible light could not directly oxidize organic compounds, accounting for the strong molecular oxygen dependent NaPCP removal with BOC-001-3 under visible light (Fig. 4a). Although NaPCP could not be oxidized by the visible

light generated holes of BOC-001-3, over 70% of NaPCP could be mineralized by the ROS generated under visible light in 8 h (Fig. S8e, ESI†). On the basis of the above results and analysis, we proposed a possible molecular oxygen activation process on the OVs of BiOCl {001} facets for the NaPCP removal under visible light (Fig. 4b). First, molecular oxygen was chemisorbed on the OVs in the transitional form of $*O_2^-$. Under visible light irradiation, molecular oxygen was then activated to $\bullet O_2^-$ through sub-band excitation, while the further reduction of $\bullet O_2^-$ favored the subsequent generation of H_2O_2 and •OH. Finally, these ROS could efficiently oxidize and mineralize NaPCP under visible light.

As BiOCl with OVs on its {001} facets could efficiently utilize visible light to activate molecular oxygen for the NaPCP removal, we further check their performance of molecular oxygen activation and NaPCP removal under solar light composed of both UV and visible light. Under solar light, the inhibition efficiencies of $\bullet O_2^-$, H_2O_2, and •OH for the NaPCP removal were estimated to be 42%, 22%, and 30%, respectively. These values were lower than those (75%, 34%, and 30%) under visible light, but much higher than those (40%, 11%, and 8%) under UV light (Fig. 3f and S8f, ESI†), suggesting that both OVs induced sub-band excitation under visible light and direct valence band to conduction band excitation under UV light took place under solar light (Fig. 4c). Moreover, the complete removal of dissolved molecular oxygen inhibited 51% of NaPCP removal, which was comparable to that of photo-generated holes, further confirming that the ROS generated over OVs on the {001} facets of BiOCl nanosheets under visible light contributed to the NaPCP removal.

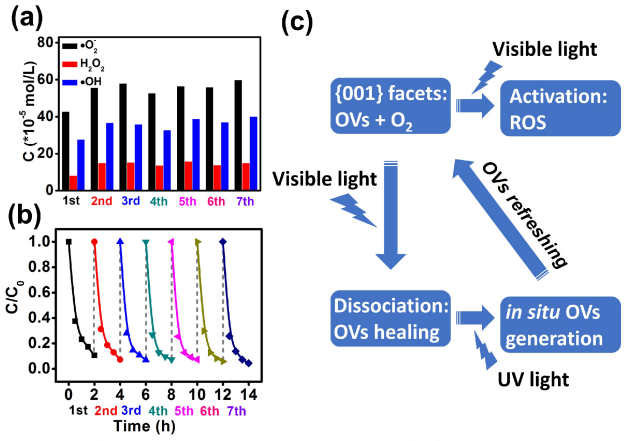

Fig. 5. Multi-cycle ROS generation (a) and photocatalytic NaPCP removal (b) with BOC-001-3 under solar light. (c) Schematic illustration of the *in situ* OVs refreshing on the {001} facets of BiOCl under solar light.

Usually OVs of oxide semiconductors would gradually be healed during their interaction with molecular oxygen,[1, 6-7] so the long term stability and the reusability of OVs are crucial for the practical environmental application. We therefore systematically evaluated the stability of BOC-001-3 and its reusability for the multi-cycle ROS generation and the NaPCP removal. It was interesting to find that the photoreactivity of BOC-001-3 did not decrease after the storage in the dark even over 7 months (Fig. S9a, ESI†), suggesting the OVs on the {001} facets of BiOCl nanosheets were very stable. However, the photoreactivity of BOC-001-3 to generate ROS and remove NaPCP gradually declined under visible light (Fig. S9b-c, ESI†). After 7 circles, BOC-001-3 only maintained 15% and 19% of its initial ROS generation and NaPCP removal efficiencies, respectively. These results confirmed that the dissociative healing of OVs simultaneously proceeded with the molecular oxygen activation on OVs, and thus significantly blocked the molecular oxygen activation channel because of surface reoxidization (Fig. S9d, ESI†). Therefore, the sustainable molecular oxygen activation with the OVs on the {001} facets of BiOCl is still a great challenge.

Very interestingly, we found the utilization of solar light was able to realize the long-term photocatalytic molecular oxygen activation and organic pollutant removal with the OVs on the {001} facets of BiOCl nanosheets. Both the ROS generation and NaPCP removal performance of BOC-001-3 under solar light did not decline even after 7 circles (Fig. 5a-b). Meanwhile, the concentration of OVs on the {001} facets was very stable, as reflected by the average percentage of $Bi^{(3-x)+}$ being kept at about 37% during repeated use (Fig. S9e, ESI†). To clarify this interesting long-term photocatalytic molecular oxygen activation of OVs on the {001} facets of BiOCl nanosheets under solar light, we prepared anatase TiO_2 nanosheets with {001} facets exposed and selectively produced OVs on the {001} facets of TiO_2 (denoted as TiO_2-001-OV) via ultra-high vacuum (UHV) treatment at 200 °C for comparison (Fig. S10a-f, ESI†). As expected, the generation of OVs on the {001} facets could also enhance the ROS generation and NaPCP removal efficiencies of anatase TiO_2 with {001} facets exposed under solar light. The NaPCP removal rate of TiO_2-001-OV was much lower than that of BOC-001-3, although the specific surface area of TiO_2-001-OV nanosheets of 10 nm in thickness was 3.3 times that of BOC-001-3 nanosheets of similar thickness (Fig. S10g and Table S1, ESI). This comparison ruled out the contribution of the particle size and the specific surface area to the higher photoreactivity of BOC-001-3 for the NaPCP removal under solar light. However, the photocatalytic ROS generation and NaPCP removal efficiencies of TiO_2-001-OV seriously declined during repeated use (Fig. S11, ESI†).

The above interesting results inspired us to gain deep insight into the UV light-induced *in situ* OVs regeneration on the facets of different oxide semiconductors. It is known that OVs can only be regenerated over TiO_2 through $Ti^{4+} + e^- \rightarrow Ti^{3+}$ reaction by UV light under UHV or O_2 deficient conditions.[19-22] Moreover, this process is energetically favorable for the OVs generation on low-coordinated removable O atoms with close interactions, such as O atoms on the O bridging rows of rutile TiO_2(110).[20] Therefore, the regeneration of OVs is infeasible due to the competitive O_2 dissociation channel for the photocatalytic aerobic oxidation of organic pollutant with TiO_2. Different from TiO_2, BiOCl can easily generate OVs on the {001} facets under UV light at ambient conditions.[9-10] First, the layered structure of BiOCl can reduce the carriers' recombination rate and facilitate the holes (h^+) being trapped at the surface lattice O along the [001] direction under UV light. The holes trapped on surface lattice O can partially neutralize the O anions through the $O^{2-} + h^+ \rightarrow O^-$ reaction, which is the first step for the OVs formation. Second, the {001} facets of BiOCl are composed of crossed bridging rows with low-coordinated and closely interacted O atoms (Fig. S12,

ESI†). The Bi-O bonds on the {001} facets are of long length and low energy and therefore favor the removal of surface O atoms.[10] Obviously, such a surface structure of BiOCl {001} facets is highly favorable for the OVs generation by further trapping h^+ with two adjacent O anions ($(O\text{-}O)^{4-}$) on the bridging rows via the $(O\text{-}O)^{4-} + 4h^+ \rightarrow O_2$ reaction, releasing O_2 and leaving behind OVs on the surface. Therefore, even though the dissociative healing of OVs on the {001} facets of BiOCl could not be avoided as that of the TiO_2 counterparts, UV light could *in situ* refresh OVs on {001} facets of BiOCl nanosheets for the sustainable visible light-driven molecular oxygen activation (Fig. 5c). As expected, after the oxidized BOC-001-3 (after the 7th cycled degradation under visible light) was refreshed by UV light for 30 min, it exhibited significantly enhanced photoreactivity for the NaPCP degradation under visible light (Fig. S12c, ESI†).

Conclusions

In conclusion, we have demonstrated that oxygen vacancies on the {001} facets of BiOCl nanosheets can more sustainably activate molecular oxygen for organic pollutant removal under solar light than the TiO_2 counterparts. The oxygen vacancies on the {001} facets of BiOCl nanosheets are effectively refreshed by UV light, and also responsible for the efficient utilization of visible light to activate molecular oxygen, accounting for their long term stability and high efficiency. These findings gain deep insight into the interaction modes of molecular oxygen with OVs, and also shed light on the importance of *in situ* OVs regeneration for long term molecular oxygen activation and organic pollutant removal with solar light.

Acknowledgements

This work was supported by National Basic Research Program of China (973 Program) (Grant 2013CB632402), National Science Foundation of China (Grants 21177048 and 51472100), Key Project of Natural Science Foundation of Hubei Province (Grant 2013CFA114), Self-Determined Research Funds of CCNU from the Colleges' Basic Research and Operation of MOE (Grant CCNU14Z01001), and Research Institute of Photocatalysis, State Key Laboratory of Photocatalysis on Energy and Environment. We also thank the National Supercomputer Center in Jinan for providing high performance computation

Notes and references

Key Laboratory of Pesticide & Chemical Biology of Ministry of Education, Institute of Environmental Chemistry, College of Chemistry, Central China Normal University, Wuhan 430079, P. R. China. E-mail: zhanglz@mail.ccnu.edu.cn; Fax/Tel: +86-27-6786 7535

† Electronic Supplementary Information (ESI) available: [details of any supplementary information available should be included here]. See DOI: 10.1039/b000000x/

1 M. A. Henderson, W. S. Epling, C. L. Perkins, C. H. F. Peden, *J. Phys. Chem. B*, 1999, **103**, 5328.
2 S. J. Tan, Y. F. Ji, Y. Zhao, A. D. Zhao, B. Wang, J. L. Yang, J. G. Hou, *J. Am. Chem. Soc.*, 2011, **133**, 2002.
3 N. G. Petrik, G. A. Kimmel, *J. Phys. Chem. Lett.*, 2011, **2**, 2790.
4 U. Aschauer, J. Chen, A. Selloni, *Phys. Chem. Chem. Phys.*, 2010, **12**, 12956.
5 M. Setvín, U. Aschauer, P. Scheiber, Y. F. Li, W. Y. Hou, M. Schmid, A. Selloni, U. Diebold, *Science*, 2013, **341**, 988.
6 Z. T. Wang, Y. G. Du, Z. Dohnalek, I. Lyubinetsky, *J. Phys. Chem. Lett.*, 2010, **1**, 3524.
7 P. P. Dholabhai, H. G. Yu, *J. Chem. Phys.*, 2013, **138**, 194705.
8 J. Jiang, K. Zhao, X. Y. Xiao, L. Z. Zhang, *J. Am. Chem. Soc.*, 2012, **134**, 4473.
9 K. Zhao, L. Z. Zhang, J. J. Wang, Q. X. Li, W. W. He, J. J. Yin, *J. Am. Chem., Soc.* 2013, **135**, 15750.
10 L. Q. Ye, L. Zan, L. H. Tian, T. Y. Peng, J. J. Zhang, *Chem. Commun.*, 2011, **47**, 6951.
11 M. Guan, C. Xiao, J. Zhang, S. Fan, R. An, Q. Cheng, J. Xie, M. Zhou, B. Ye, Y. Xie, *J. Am. Chem. Soc.*, 2013, **135**, 10411.
12 X. Zhang, Z. H. Ai, F. L. Jia, L. Z. Zhang, *J. Phys. Chem. C*, 2008, **112**, 747-753.
13 H. Li, L. Z. Zhang, *Nanoscale*, 2014, **6**, 7805.
14 F. Zuo, L. Wang, T. Wu, Z. Y. Zhang, D. Borchardt P. Y. Feng, *J. Am. Chem. Soc.*, 2010, **132**, 11856.
15 M. Liu, X. Q. Qiu, M. Miyauchi, K. Hashimoto, *Chem. Mater.*, 2011, **23**, 5282.
16 I. Justicia, P. Ordejón, G. Canto, J. L. Mozos, J. Fraxedas, G. A. Battiston, R. Gerbasi, A. Figueras, *Adv. Mater.*, 2002, **14**, 1399.
17 L. R. Grabstanowicz, S. Gao, T. Li, R. M. Rickard, T. Rajh, D. J. Liu, T. Xu, *Inorg. Chem.*, 2013, **52**, 3884.
18 Y. F. Li, A. Selloni, *J. Am. Chem. Soc.*, 2013, **135**, 9195.
19 W. J. Lo, Y. W. Chung, G. A. Somorjai, *Surf. Sci.*, 1978, **71**, 199.
20 S. Mezhenny, P. Maksymovych, T. L. Thompson, O. Diwald, D. Stahl, S. D. Walck, J. T. Yates, *Chem. Phys. Lett.*, 2003, **369**, 152.
21 J. G. Highfield, M. *J.* Grätzel, *Phys. Chem.*, 1988, **92**, 464.
22 R. Wang, N. Sakai, A. Fujishima, T. Watanabe, K. Hashimoto, *J. Phys. Chem. B*, 1999, **103**, 2188.